

Document downloaded from:

<http://hdl.handle.net/10251/157304>

This paper must be cited as:

Díaz-Fernández, F.J.; Pinilla-Cienfuegos, E.; García Meca, C.; Lechago-Buendia, S.; Griol Barres, A.; Martí Sendra, J. (2019). Characterisation of on-chip wireless interconnects based on silicon nanoantennas via near-field scanning optical microscopy. IET Optoelectronics. 13(2):72-76. <https://doi.org/10.1049/iet-opt.2018.5071>



The final publication is available at

<https://doi.org/10.1049/iet-opt.2018.5071>

Copyright Institution of Electrical Engineers

Additional Information

This paper is a postprint of a paper submitted to and accepted for publication in IET Optoelectronics and is subject to Institution of Engineering and Technology Copyright. The copy of record is available at IET Digital Library.

Characterization of On-Chip Wireless Interconnects Based on Silicon Nanoantennas via Near-Field Scanning Optical Microscopy

Francisco J. Díaz-Fernández*, Elena Pinilla-Cienfuegos, Carlos García-Meca, Sergio Lechago, Amadeu Griol, Javier Martí

Nanophotonics Technology Center, Universitat Politècnica de València, 46022, Valencia, Spain

*fradafer@ntc.upv.es

Abstract: Recently, a novel Photonic Integrated Circuit (PIC) paradigm based on the use of a new kind of ultra-directive, low-loss, highly-efficient and broadband silicon nanoantenna has enabled the first demonstration of an on-chip wireless interconnect, with potential applications in reconfigurable networks and lab-on-a-chip systems. Despite the fact that the far-field properties of these nanoantennas have been widely studied, their near-field behaviour stays unexplored. In this work, we study this feature through scanning near-field optical microscopy (SNOM). For this purpose, we design and characterize an on-chip 2-port wireless link using a tailored SNOM. The conducted near-field measurements will be useful to improve the design of these integrated photonic devices with potential impact on a variety of applications, from biosensing to optical communications.

1. Silicon Nanoantennas: Introduction

On-chip optical interconnects have proved to overcome the ever-increasing power consumption and restricted throughput of the copper-based electronic nanowires mostly used in large-scale integration systems. As a consequence, PICs will be crucial for high-performance computing, ultra-fast networks, and lab-on-a-chip devices [1, 2], especially in areas such as spectroscopy [3] or biomedicine [4]. These demanding applications will require novel features, such as dynamically-reconfigurable light pathways, as well as an on-chip control of optical radiation, due to the stringent design rules and limited on-chip reconfigurability of wired schemes, which usually lead to complex topologies and large footprints [5,6]. Furthermore, current on-chip waveguide-based structures cannot provide the far-field light-target interaction required by a number of sensing devices [7-9]. In the same way as radio frequency and microwave antennas have enabled a myriad of applications (in a wide range of fields, from telecommunications to biomedical image, for instance), on-chip wireless devices promise to overcome a number of current PIC limitations, paving the way to a broad assortment of new functionalities.

Most studies on wireless on-chip devices are based on the use of plasmonic nanoantennas [10-17] made up of metals such as gold or silver, which can constitute an efficient solution in some applications belonging to the fields of spectroscopy or optical sensing, as a consequence of their ability to concentrate electromagnetic fields. However, plasmonic nanoantennas do not normally yield an optimal staging when trying to establish non-guided communications or data transmission in the near-infrared wavelengths, as a result of their poor radiation properties and high metallic absorption at optical frequencies. The radiation ability of silicon particles has been demonstrated in different studies [17, 18], establishing the superior efficiency of silicon nanoantennas in comparison with plasmonic ones.

Recently, a novel PIC paradigm based on the use of a new kind of ultra-directive (directivity higher than 150), low-loss,

highly-efficient (total efficiency close to 90%) and broadband silicon nanoantenna has been proposed [19]. Moreover, these dielectric antennas employ silicon as the constituent material, which assures their compatibility with the Complementary Metal-Oxide-Semiconductor (CMOS) technology. This alternative platform has enabled new on-chip applications, including reconfigurable networks and ultra-integrated biomedical devices. While the far-field behaviour of the aforementioned antennas (e.g., directivity and radiation efficiency) has been deeply studied [19], their near-field properties remain mostly unexplored. Here, we fabricate (see section 3) and thoroughly study the near-field behaviour of this kind of antenna both numerically and experimentally (see section 6). This study paves the way to the design and improvement of new integrated photonic devices. All designs and experiments correspond to a wavelength $\lambda = 1550$ nm.

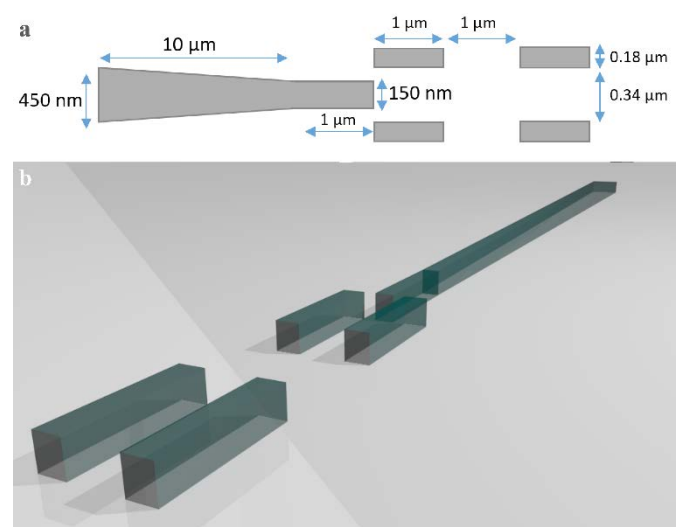


Fig. 1. (a) Schematic top view of the antenna and directors. (b) 3D representation of the antenna used to build the studied links.

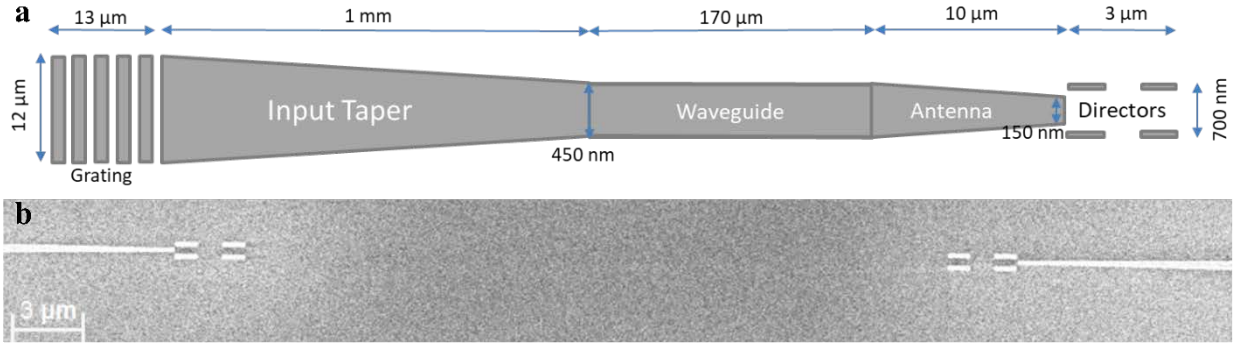


Fig. 2. (a) Schematic top view of the vertical coupler grating, waveguides and nanoantenna. (b) Scanning Electron Microscope (SEM) image of the fabricated 2-port-link.

2. Nanoantenna design

Following the work in [19], we study a silicon nanoantenna consisting of a 10-μm-long inverted-taper (see Fig. 1a). This nanoantenna is already able to radiate the field with a directivity higher than 50. Nonetheless, to further improve the directivity of the inverted taper nanoantenna while maintaining a reduced footprint, we added different planar structures working as directors (in the same way as in typical Yagi-Uda antennas [20]). Specifically, each director is made up of two silicon strip pieces. The full antenna is shown in Fig. 1. To analyse the response of this nanoantenna, 3D simulations were performed with the commercial software CST Microwave Studio. The results show an extremely high directivity with one, two and three pairs of directors (with the directivity increasing as the number of director pairs grows) [19]. While the three-pair configuration provides the highest directivity, the improvement with respect to the two-pair configuration is not too high (~33%). For this reason, we chose an inverted-taper antenna followed by two pairs of directors as the structure under study, since this configuration already satisfies the directivity requirements of our experiment (see below) and simplifies the design and fabrication of the sample. To enable not only the near-field characterization of the proposed antennas but also a far-field testing (see section 4), we chose a basic 2-port nanolink consisting of two identical antennas with a gap distance d between them (see Fig. 2).

Note that the performance of the nanolink in terms of power efficiency is maximised when the nanoantennas are covered with a thick SiO₂ layer. Therefore, this is a basic requirement for low-loss high-speed data transmission applications. However, this thick SiO₂ layer entails a strong limitation concerning near-field measurements, since the intensity of the evanescent field of the mode supported by this structure is too weak. To mitigate this problem, we performed different simulations of the optical response of the nanolink as a function of the thickness of the SiO₂ layer. We chose the minimum thickness of this layer (220 nm) that ensured a similar behaviour of the near-field intensity through all the elements of the nanolink, while keeping a sufficient long-distance transmission capacity so as to allow the aforementioned far-field characterization.

Throughout the whole study, we operate in TE mode. In this respect, the width of the silicon waveguides carrying light

to/from the nanoantennas (450 nm) was designed to operate in monomode regime.

With these considerations in mind, we designed and fabricated a sample containing three different nanolinks (labelled as Link a, Link b, and Link c) with a gap $d = 30 \mu\text{m}$, allowing us to verify the repeatability of the process. Input and output grating couplers [21, 22] enabled vertical light injection (extraction) to (from) the chip. The connection between the nanoantennas and the gratings was performed via tapered waveguides (see Fig. 2a).

3. Fabrication

The silicon antennas, grating couplers and waveguides were fabricated over standard silicon-on-insulator (SOI) samples from SOITEC wafers with a top silicon layer thickness of 220 nm (resistivity $\rho \sim 1\text{-}10 \Omega \cdot \text{cm}^{-1}$, with a lightly p-type background doping of $\sim 10^{15} \text{ cm}^{-3}$) and a buried oxide layer thickness of 220 nm. The fabrication is based on an electron-beam direct-writing process, CMOS-compatible, performed on a coated 100-nm hydrogen silsesquioxane (HSQ) resist film. This electron-beam exposure was performed with a Raith150 tool and has been optimized to reach the required dimensions employing an aperture size of 30 μm with an acceleration voltage of 30 KeV. After developing the HSQ resist using tetramethylammonium hydroxide, the resist patterns were transferred into the SOI samples using fluoride gases via an optimized inductively coupled plasma-reactive ion etching process. Finally, a 220 nm-thick silicon dioxide upper cladding was deposited on the SOI sample by using a plasma-enhanced chemical vapor deposition system from Applied Materials. To ensure the correct fabrication of the sample, Scanning Electron Microscope (SEM) images were taken, focusing on the nanolinks and the directors of the nanoantennas (see Fig. 2b).

4. Far-field Characterization

Prior to the study of its near-field behaviour, the link was characterized in the far field to verify its correct performance. In particular, the link power efficiency $\eta_p = P_{\text{RX}}/P_{\text{TX}}$ (P_{RX} and P_{TX} are the received and transmitted power, respectively) of the three fabricated 30-μm-long nanolinks was experimentally measured. For this purpose, an External Cavity Laser (ECL) was employed to inject light to the input vertical

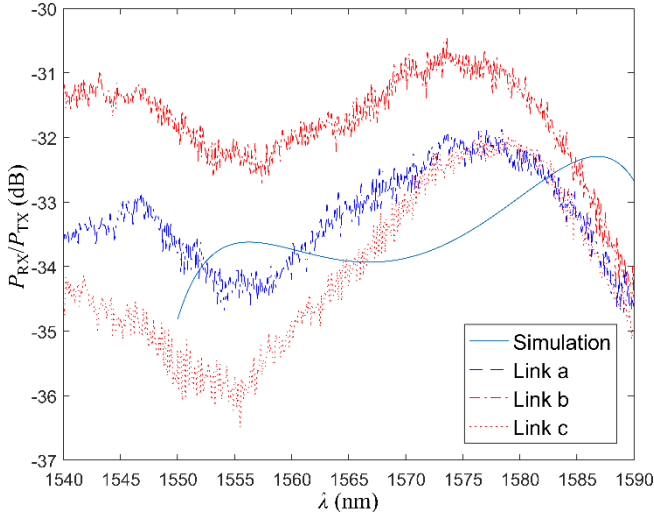


Fig. 3. Experimental (dashed (Link a), dashed-dotted (Link b) and dotted (Link c)) and theoretical (solid) power efficiency η_P of the different fabricated links.

gratings of the sample via an optical fibre at wavelengths of 1540-1590 nm. The signals exiting the output gratings were received with a photodetector. Maximum power efficiency was ensured by optimizing the polarization of the signal and through the previous alignment of the input and output fibres with the help of an optical microscope.

As a reference, η_P was also simulated using CST Microwave Studio (see Fig. 3). According to the simulations, the power efficiency should be around -34 dB for a wavelength of 1550 nm, showing a good agreement with the experimental results (see Fig. 3). It is worth mentioning that an additional structure consisting of two vertical grating couplers linked by an almost lossless 12- μm -wide waveguide was measured to quantify the experimental loss introduced by the grating couplers. This loss was subtracted from the measured values of η_P to allow a direct comparison with the simulation.

Note that the SiO_2 layer employed to cover the 30- μm -long links was significantly thinner than in previous designs [19] (220 nm vs 2 μm) to allow a near-field characterization of the device, which resulted in a lower link power efficiency. A frequency shift between the experimental and theoretical results is noticed, which might be a result of deviations introduced in the fabrication process. In particular, the plasma-enhanced chemical deposition technique used to build the 220-nm SiO_2 layer that covers the sample and the

free-space link gap is prone to introduce small air bubbles within it, giving rise to inhomogeneities in the aforementioned free-space region, which can alter its optical response. Secondly, since the upper surface of this SiO_2 layer coincides with that of the antennas (where the field intensity is higher), the effect of its roughness can be significant as compared to a typical (thicker) cover layer. Finally, some imbalances caused by the exposure field of the e-beam when lithographing the nanolinks may happen, providing slightly altered gap distances or antenna misalignments. In any case, the good agreement observed in terms of power efficiency assures the expected radiation behaviour of the nanoantennas, and hence the presence of the sought near field to be explored via SNOM technology, which is the core idea of our study.

5. SNOM Setup

SNOM measurements were performed with a commercial MultiView 4000 system (Nanonics Imaging Ltd.) working in collection mode. A bent fibre tip (Nanonics Imaging Ltd) with a 400 nm aperture, Cr/Au coated, pre-mounted on a tuning-fork working in tapping mode at 36.94 kHz was used to scan the lithographed sample while it was kept fixed (see Fig. 4a). The sample was vertically illuminated with an optical fibre mounted on a 3D stage. Since the vertical grating coupler has been designed to couple light at 11° , we achieved this angle using an adjustable angle mounting plate (see Fig. 4b). The whole system (sample, input fibre and SNOM tip) could be pre-visualized with a vertical optical microscope that enables a correct fibre-sample alignment and an accurate positioning of the SNOM probe on top of the lithographed structures (a sketch of the setup can be seen in Fig. 4c). The optical fibre was connected to a tuneable laser (EXFO FLS-2600) at a fixed light polarization and a power of 0 dBm ($\lambda = 1550$ nm). The SNOM was controlled through the Nanonics Imaging Ltd Software and the near-field signal was detected using a FWPR-S Femtowatt Photoreceiver.

6. Near-field Simulations & Measurements

To guide and verify the SNOM characterization, we first studied numerically the near-field behaviour of the fabricated nanoantennas via CST Microwave Studio for a wide range of vertical distances. The near-field intensity was

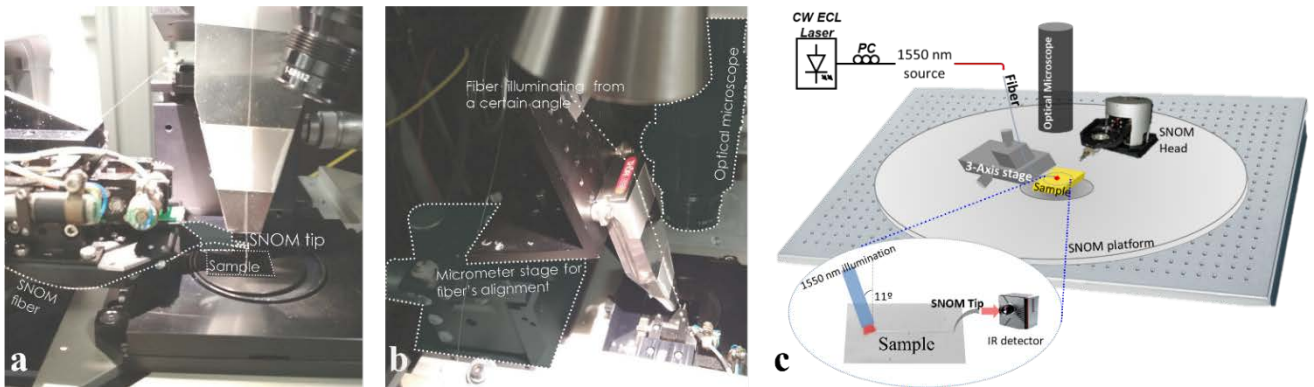


Fig. 4. (a) Schematic view of the setup. (b)(c) Pictures of the setup.

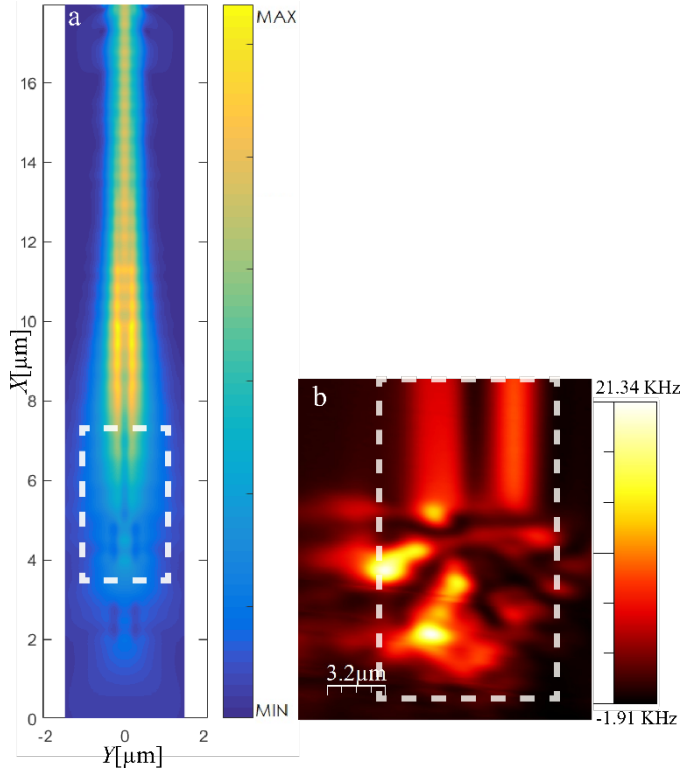


Fig. 5. Simulated (a) and measured (b) near-field intensity above the emitting antenna. Areas enclosed by dashed lines represent the same region in both images.

collected by the SNOM working in collection mode, with the tip placed perpendicular to the sample, allowing a mode matching between the tip and the measured structures [23, 24]. Measurements at different vertical distances z_{LIFT} over the sample were performed. Particularly the SNOM tip was placed at $z_{\text{LIFT}} = 0.1 \mu\text{m}$ and $z_{\text{LIFT}} = 0.4 \mu\text{m}$. The details for each case are discussed below. The measured images were edited using the WSxM Scanning Probe Microscopy Software [25].

6.1. Constant plane $z_{\text{LIFT}} = 0.1 \mu\text{m}$

In this case, the SNOM tip was retracted 100 nm over the sample, allowing us to operate in lift mode, scanning a constant plane without risk of crashing the probe due to irregularities at the sample topography (resulting from the lack of planarization after the fabrication process).

6.1.1. Emitting antenna: As expected, the simulation results show an electric field concentration at the inverted-taper. Additionally, a slight field concentration can also be identified between the first pair of directors (see Fig. 5a). However, the corresponding measurements of the fabricated emitting antenna showing the electric field radiation between the first pair of directors were not in good agreement with the simulations (see Fig. 5b). These divergences could be attributed to fabrication failures, and the lack of planarization previously mentioned. It is worth mentioning that this discrepancy was solved by raising the tip height, as detailed in section 6.2.

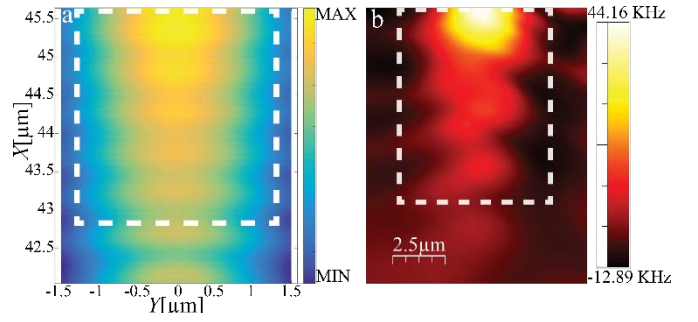


Fig. 6. Simulated (a) and measured (b) near-field intensity propagated between antennas. Areas enclosed by dashed lines represent the same region in both images.

6.1.2. Propagation: The SiO_2 region between the emitting and receiving antennas was studied at a retracted tip height of $0.1 \mu\text{m}$, giving us a portrait of the electric field propagation. The simulated radiated field distribution (see Fig. 6a) was recognizable in the performed SNOM measurement (see Fig. 6b). This information could be exploited to obtain the radiation features of the antenna without demanding far-field characterization.

6.1.3. Grating: Furthermore, near-field intensity was measured in the output grating (see Fig. 7). Even though the vertical grating was designed to work at 11° , and that the SNOM tip was perpendicular to the sample, we were able to verify the field concentration at the centre of the grid, confirming the correct behaviour of this device.

6.2. Constant plane $z_{\text{LIFT}} = 0.4 \mu\text{m}$

6.2.1. Emitting antenna: The differences seen between the simulation and the measurement close to the sample at a tip height of $0.1 \mu\text{m}$ disappeared when raising the SNOM tip to $0.4 \mu\text{m}$. In this case, the measurement above the directors of the emitting antenna showed the typical field concentration of this kind of element, in good agreement with the numerical simulation (see Fig. 8).

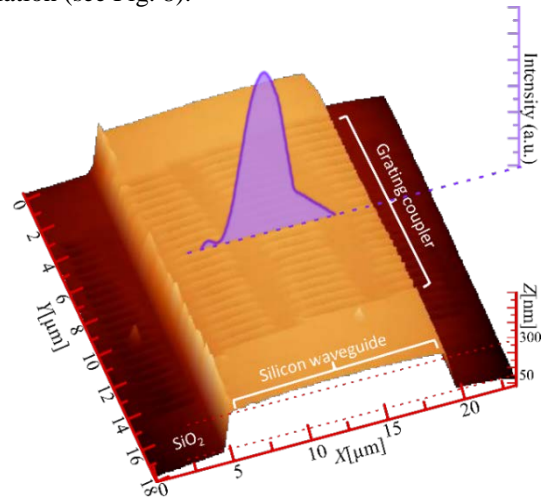


Fig. 7. 3D representation of the AFM image of the grating coupler. In purple, near-field intensity measured at a distance of $0.1 \mu\text{m}$ above the grating coupler.

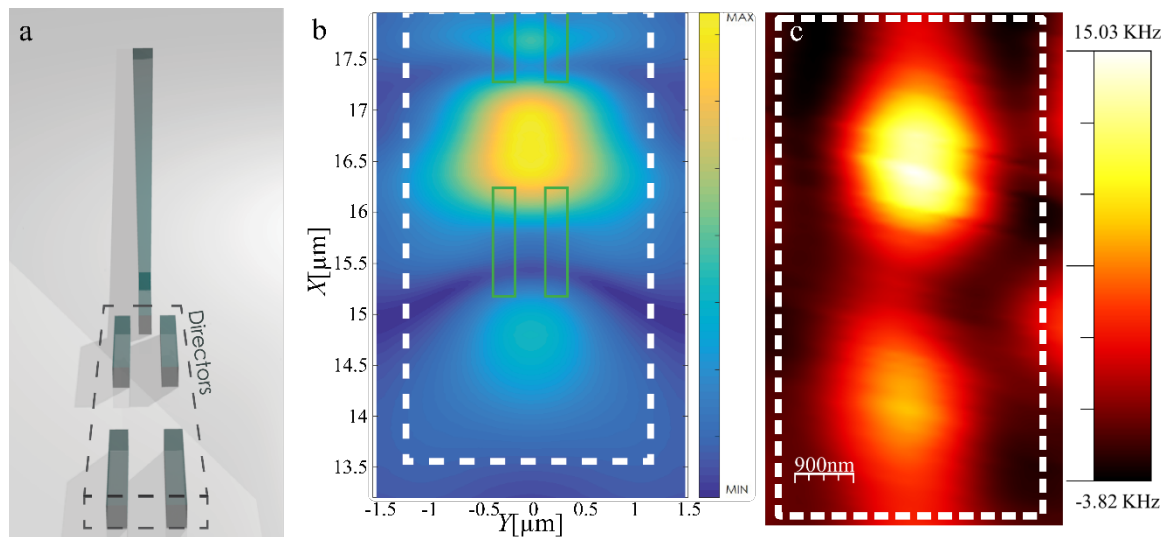


Fig. 8. (a) Top view representation of the emitting antenna. Simulated (b) and measured (c) near-field intensity above the fabricated emitting antenna between directors. Areas enclosed by dashed lines represent the same region in all images.

7. Conclusion

Our results show for the first time the near-field response of an on-chip wireless link, shedding light on its fundamental underlying mechanisms. This additional information will be useful to improve the design and optimization processes of these integrated photonic devices and could lead to the development of new applications in a variety of fields.

As future work, it might be interesting to improve the near-field measurements by using a thinner SNOM tip and taking into account the tilt of the SNOM tip.

Finally, this first approach to the near-field characterization in radiating elements at the nanoscale will pave the way to the analysis of other advanced integrated photonic devices such as lab-on-a-chip sensors or wireless on-chip networks.

8. Acknowledgments

Funding support from the Spanish Ministry of Economy and Competitiveness under grants TEC2015-63838-C3-1-R OPTONANOSENS (MINECO/FEDER, UE) and TEC2015-73581-JIN PHUTURE (AEI/FEDER, UE), the EU-funded H2020-FET-HPC EXANEST (No.671553) and the Generalitat Valenciana's PROMETEO grant NANOMET PLUS (PROMETEO II/2014/34) are acknowledged. E.P.-C. acknowledges support from Generalitat Valenciana under Grant APOSTD/2016/025.

We thank David Zurita for his help in the assembly of the SNOM setup.

9. References

- [1] Kirchain R., Kimerling, R.: 'A roadmap for nanophotonics', Nat. Photonics, 2007 vol. 1. pp 303-305
- [2] Zhang Y.S., Watts B.R., Guo T.Y., et al.: 'Optofluidic device based microflow cytometers for particle/cell detection: a review', Micromachines, 2016. 7(4), 70
- [3] Redding B., Liew S.F, et al.: 'Compact spectrometer based on a disordered photonic chip' Nat. Photon., 2013, 7(8), 746–751
- [4] Fan X. D., White I. M.: 'Optofluidic microsystems for chemical and biological analysis', Nat. Photon, 2011, 5(10), 591–597
- [5] Condrat C., Kalla P., Blair S.: 'Crossing-aware channel routing for integrated optics', IEEE Transactions on Computer-Aided Design of Integrated Circuits and Systems, 2014, 33, 814–825
- [6] Lee B.G, Rylyakov A.V, Green W.M.J., et al.: 'Monolithic silicon integration of scaled photonic switch fabrics, CMOS logic, and device driver circuits', J Lightw Technol, 2014, 32: 743–751
- [7] Robinson J.P, Roederer M.: 'Flow cytometry strikes gold', Science, 2015, 350: 739–740.
- [8] Mao X.L., Nawaz A.A., Lin S.C., et al.: 'An integrated, multiparametric flow cytometry chip using 'microfluidic drifting' based three-dimensional hydrodynamic focusing', Biomicrofluidics, 2012, 6: 024113.
- [9] Schurr J.M.: 'Dynamic light scattering of biopolymers and biocolloids', CRC Crit Rev Biochem 1977, 4: 371–431.
- [10] Maksymov S., Davoyan A., Kivshar Y.: 'Enhanced emission and light control with tapered plasmonic nanoantennas', App. Phys. Lett., 2011 vol. 99
- [11] Brongersma M. L.: 'Plasmonics: Engineering optical antennas', Nat. Photon, 2008, 2(5), 270–272
- [12] Alù A., Engheta N.: 'Wireless at the Nanoscale: Optical Interconnects using Matched Nanoantennas', Phys. Rev. Lett., 2011 104, 213902
- [13] Novotny L., van Hulst N.: 'Antennas for light', Nat. Photon. 2011, 5(2), 83–90
- [14] Giannini V., Fernández-Domínguez A.I, et al.: 'Plasmonic Nanoantennas: Fundamentals and Their Use in Controlling the Radiative Properties of Nanoemitters', Chem. Rev., 2011, 111(6), 3888–3912

- [15] Espinosa-Soria A., Pinilla-Cienfuegos E., Díaz-Fernández F.J., et al.: 'Coherent Control of a Plasmonic Nanoantenna Integrated on a Silicon Chip', ACS Photonics Article ASAP DOI: 10.1021/acsp Photonics.8b00447
- [16] Bellanca B., Calò G., Kaplan A. E., et al.: 'Integrated Vivaldi plasmonic antenna for wireless on-chip optical communications', Opt. Express, 2017, 25, 16214-16227
- [17] Krasnok A.E., Miroshnichenko A.E., et al.: 'All-dielectric optical nanoantennas', Opt Express 2012, 20: 20599–20604
- [18] Krasnok A.E., Simovski R., Belov P.A., et al.: 'Superdirective dielectric nanoantennas', Nanoscale, 2014, 6 (13), 7354 - 7361
- [19] García-Meca C., Lechago S., et al.: 'On-chip wireless silicon photonics: from reconfigurable interconnects to lab-on-chip devices', Light Sci. Appl., 2017, vol. 6, pp. e17053
- [20] Kosako T., Kadoya Y., Hofmann H.F.: 'Directional control of light by a nano-optical Yagi-Uda antenna', Nat Photonics, 2010, 4: 312–315
- [21] Sun J., Timurdogan E., Yaacobi A., et al.: 'Large-scale nanophotonic phased array', Nature, 2013, 493(7431), 195–199
- [22] Van Acoleyen K., Rogier H., Baets R.: 'Two-dimensional optical phased array antenna on silicon-on-insulator', Opt. Express, 2010, 18(13), 13655–13660
- [23] Dvořák P., Édes Z., Kvapil M., et al.: 'Imaging of near-field interference patterns by aperture-type SNOM – influence of illumination wavelength and polarization state', Opt. Express, 2017, 25, 16560-16573
- [24] Bazylewski, P., Ezugwu, S., Fanchini, G.: 'A Review of Three-Dimensional Scanning Near-Field Optical Microscopy (3D-SNOM) and Its Applications in Nanoscale Light Management', Appl. Sci. 2017, 7, 973.
- [25] Horcas I., Fernandez R., Gomez-Rodriguez J.M., et al.: 'WSXM: a software for scanning probe microscopy and a tool for nanotechnology', Rev. Sci. Instrum., 2007, 78, 013705